Single-Source Pulsed Laser Deposited Perovskite Solar Cells with >19% Efficiency

Tatiana Soto-Montero
University of Twente https://orcid.org/0000-0002-3538-0002
Suzana Kralj
University of Twente https://orcid.org/0000-0003-2847-8359
Randi Azmi
KAUST https://orcid.org/0000-0002-8518-9388
Manuel A. Reus
Technical University of Munich https://orcid.org/0000-0003-0508-6694
Junia S. Solomon
University of Twente https://orcid.org/0000-0002-0656-6318
Daniel M. Cunha
University of Twente https://orcid.org/0000-0002-8217-2580
Wiria Soltanpoor
University of Twente https://orcid.org/0000-0002-2749-7593
Drajad Satrio Utomo
KAUST
Esma Ugur
KAUST https://orcid.org/0000-0003-0070-334X
Badri Vishal
KAUST https://orcid.org/0000-0002-3480-6841
Martin Ledinsky
FZU – Institute of Physics of the Czech Academy of Sciences https://orcid.org/0000-0002-6586-5473
Peter Müller-Buschbaum
Technische Universität München https://orcid.org/0000-0002-9566-6088
Finn Babbe
Lawrence Berkeley National Laboratory: Berkeley, US https://orcid.org/0000-0002-9131-638X
Do Kyoung Lee
Molecular Foundry Division, Lawrence Berkeley National Laboratory
Carolin M. Sutter-Fella
Molecular Foundry Division https://orcid.org/0000-0002-7769-0869
Erkan Aydin
KAUST https://orcid.org/0000-0002-8849-2788
Stefaan De Wolf

KAUST https://orcid.org/0000-0003-1619-9061
Monica Morales-Masis (m.moralesmasis@utwente.nl)
University of Twente https://orcid.org/0000-0003-0390-6839

Research Article

Keywords: single-source, pulsed laser deposition, metal halide perovskites, passivation, perovskite solar cells, vapor deposition

Posted Date: November 29th, 2023

DOI: https://doi.org/10.21203/rs.3.rs-3671187/v1

Abstract

Single-source vapor deposition of metal halide perovskites has, to date, remained challenging due to the dissimilar volatilities of the perovskite precursors, limiting the controlled transfer of multiple elements at once. Here, we demonstrate that pulsed laser deposition (PLD) addresses the rate-control challenges of single-source evaporation, enabling solar cells with power conversion efficiencies above 19%. We combined dry mechanochemical synthesis and PLD to fabricate $MA_{1-x}FA_xPbI_3$ and Cl-passivated $MA_{1-x}FA_xPbI_3$ films from a single-source target. The films are grown onto hole-selective self-assembled monolayers, where first a thin PbI_2-rich layer forms, leading to full perovskite conversion. Onto the perovskite, an oleylammonium iodide (OAmI) post-treatment is then applied to passivate its top surface by forming a 2D perovskite film. When incorporating $PbCl_2$ in the target and OAmI-based 2D passivation, a remarkable 19.7% efficiency for p–i–n perovskite solar cells is achieved with enhanced device stability. This highlights the appeal of PLD to fully unlock the potential of single-source vapor-deposited perovskite towards low-cost and efficient photovoltaics.

Main

Metal halide perovskites (MHPs) have proven excellent, tunable optoelectronic properties and can be processed through a large variety of thin-film fabrication methods, promising cost-effective, high-efficiency photovoltaics.[1] Yet, vapor phase deposition of MHPs remains much less explored than solution-based processes. Nevertheless, vapor phase deposition of semiconductors dominates in commercial thin-film PV and other optoelectronic devices manufacturing, with proven scalability, avoiding toxic solvents and offering precise control over film thickness and conformality, which is important when depositing on non-planar surfaces, such as textured substrates.[2] However, in the case of MHPs, a clear challenge of vapor phase deposition lies in the large dissimilarity in the volatilities of the MHP precursors. To date, this has represented a clear roadblock towards the development of effective single-source single-step evaporation approaches. The complexity further increases as the compositions of perovskite solar cells (PSCs) with demonstrated high power conversion efficiencies (PCEs)[3] are based on mixtures of at least two different cations and even three different halide anions in the stoichiometry for their MHP photo-absorber.[4–6] Pulsed laser deposition (PLD) has emerged as a method with the particular advantage of near-stoichiometric transfer of multiple elements from a solid target, already well demonstrated for complex perovskites oxides in the past.[7] More recently, promising results were obtained as well for various halide perovskite materials. In both cases, the single source is composed of mechanochemically synthesized precursor powders pressed into a target.[8–11] For MHPs, careful adjustment of a non-stoichiometric target (with organic-rich composition) and deposition parameters results in high-quality perovskite films of the desired stoichiometry.[11,12] Furthermore, wafer-sized deposition via PLD is achievable with state-of-the-art hardware configurations.[13,14]

Previously, our group demonstrated the controlled growth of $MA_{0.55}FA_{0.45}PbI_3$ thin films on a 30 ´ 30 mm^2 area along with the successful integration of the as-deposited absorber in *n–i–p* PSCs (in such

devices, the perovskite (*i*-layer) is deposited onto the electron-selective contact (*n*-layer), followed by the deposition of the hole-selective contact (*p*-layer)).[12] These proof-of-concept devices have shown a modest PCE of 14%, primarily constrained by a low open circuit voltage (V_{OC}) and fill factor (FF). These limitations are attributed to non-radiative recombination losses emerging from defects in the bulk and at the top surface of the as-deposited MHP.[15] The latter, together with a high series resistance resulting from suboptimal carrier-selective contacts and interfaces, prevented higher device performance. Even though further growth optimization of the MHP absorber by PLD is required to reduce the defect density, non-radiative recombination losses are inherent to polycrystalline MHPs,[16] which mandates the development of additive and post-treatments to passivate the remaining defects. To date, most passivation strategies have been developed for solution-based perovskites, improving PSCs to their current performance records.[17] Yet, it is evident that vapor-deposited perovskites can also benefit from passivation approaches, as demonstrated recently by Yu-Hsien *et al.* for thermally co-evaporated MHP.[18]

Herein, we implement two strategies to improve the quality of the PLD-grown MHP absorber and enhance their PCE at the device level. The approach consists of the growth of $MA_xFA_{1-x}PbI_3$ thin films on an inverted device architecture (*p–i–n*, where now first the *p*-layer is deposited). These inverted PSCs are arguably easier to fabricate and scale up than their *n–i–p* counterparts.[1] Furthermore, carbazole-based self-assembled monolayers (SAMs), specifically 2PACz ([2-(9H-Carbazol-9-yl)ethyl]phosphonic acid) when employed as hole-collective contacts, ensure minimal parasitic optical absorption losses.[19] Our first strategy involves bulk passivation by introducing $PbCl_2$ as a fourth precursor to the single source PLD target, containing tunable ratios of MAI: FAI: PbI_2: $PbCl_2$. Previous works demonstrated the enhanced charge carrier lifetimes and, thus, improved PCE of co-evaporated PSCs with the addition of $PbCl_2$ as a third or fourth precursor.[20,21] However, while co-evaporation demands independent control of three or four separate evaporation sources, PLD uses a single target containing all the required precursors. Further, as a second strategy we applied a 2D layered perovskite on the $MA_{1-x}FA_xPbI_3$ and Cl-passivated $MA_{1-x}FA_xPbI_3$ perovskite surface, obtained through an oleylammonium iodide (OAmI) post-treatment[22] and confirmed via *in-situ* photoluminescence (PL). Quasi-fermi level splitting (QFLS) analysis of the final PSCs predicts that the addition of $PbCl_2$ during growth could lead to a V_{OC} increase of ~27 mV, that could further be enhanced from ~1.07 to ~1.15 V by the addition of the 2D passivation layer. The addition of Cl^- also benefits the device fill factor (FF). Combined, this resulted in a remarkable boost in PCE to 19.7% and an 85% PCE retention after 1000 h at 85 °C. Our work not only demonstrates the highest PCE (to the best of our knowledge) for single-source vapor-deposited PSCs but also highlights the synergetic effect of bulk and interface passivation in enhancing the performance and stability of devices containing single-source vapor-deposited perovskite absorbers.

PLD of multi-compound metal halide perovskites

Fig. 1a presents a simplified illustration of the PLD process for the growth of MHP. During this process, argon (Ar) gas is introduced to the vacuum chamber to precisely control the deposition pressure during

the laser ablation of the source material. The optimized deposition pressure (0.02 mbar) plays a key role in shaping the plasma plume and the transfer of the MHP precursors from the target toward the substrate pulse-by-pulse.[11] This transfer is initiated as laser photons interact with the target material via excitation of bound electrons and subsequent transfer of their energy to the lattice of the target material through electron-phonon coupling, facilitating thermalization processes. Thus, the key strength of this method lies in its unique ability to transfer the integrated constituents from a dense and homogeneous single target into a confined plasma plume.[23] This effectively addresses the volatility challenges encountered in single-source thermal evaporation methods. Excess of the lighter or volatile components compensates for the material loss at the edges of the plume. In contrast, heavier or less volatile elements exhibit forward-directed transfer within the confined plasma plume.[12] Moreover, mechanochemical synthesis is a solvent-free, high-yield method that triggers the initial solid-state reaction of the precursors and promotes the homogeneous distribution of all precursors in the powder mixture.[24] The final perovskite/precursors powder mixture is pressed into a target (MAI: FAI: PbI_2, 6 : 2 : 1) that, from now on, is referred to as the single source.

Fig. 1b shows the specular X-ray diffraction (XRD) pattern of $MA_{1-x}FA_xPbI_3$ thin films grown on freshly coated 2PACz-SAMs on ITO substrates, showing the orientations on the (100) and (111) family planes. Incorporating a slight amount of PbI_2 can be tuned via minor deposition pressure adjustments.[12] Fig. 1c, shows the PL emission peak at ~1.58 eV, which exhibits a subtle redshift compared to the previous $MA_{1-x}FA_xPbI_3$ films grown on SnO_2/PCBM surfaces.[12] To understand this shift, we analyzed the N 1s core levels using X-ray photoelectron spectroscopy (XPS) as depicted in Fig. 1d, revealing a cation ratio of ~ 44:56 MA^+: FA^+. The calibration of target composition *vs* final film composition has been described in detail in our earlier work.[12] The morphology of the thin films is shown in Fig. 1e, revealing a predominantly compact columnar growth from the first 20 nm onwards. Nevertheless, further enhancements in the growth process are required to achieve a void-free structure for thicker films.

Growth mechanism: GIWAXS of $MA_{1-x}FA_xPbI_3$ thin films

The growth of MHP by co-evaporation and sequential evaporation processes has been discussed previously, suggesting a preferential sticking to the substrate of the inorganic component, PbI_2, followed by reaction and interdiffusion of organic molecules throughout the inorganic template to convert and form high-quality MHP films.[25,26] To better understand these mechanisms for PLD-grown $MA_{1-x}FA_xPbI_3$ thin films, we performed depth-dependent GIWAXS at the DESY synchrotron by incident angle variation.[27] Three different incident angles α were chosen to extract depth-dependent information on microstructural changes with a particular focus close to the ITO/2PACz-SAMs/perovskite interface (α_1=0.4°, above the critical angle of the perovskite), the perovskite bulk (α_2=0.2°), and the surface (α_3=0.16°, well below the critical angle of the perovskite). Fig. 2a presents the GIWAXS data acquired from a 20 nm sample after one complete deposition scan. Intense signals corresponding to the ITO substrate, highlighted with arrows, alongside the presence of PbI_2 and the perovskite (100) family crystal planes throughout the

bottom interface, bulk, and surface are observed at the initial stages of growth. Fig. 2b shows a reduction in PbI_2 intensity primarily present at the bottom interface of 100 nm thick films, accompanied by the emergence of other perovskite family peaks, including (111), (110), and (210). Lastly, Fig. 2c displays the complete conversion of a 400 nm thick perovskite film after 18 deposition scans with partially ordered preferential (111) orientation parallel to the substrate. Supplementary Fig. 1 provides additional insights through pseudo-XRD analysis for all three scenarios. These findings corroborate our previous assumptions concerning the MHP formation process on amorphous substrates during PLD, characterized by the initial preferential adhesion of PbI_2 followed by interdiffusion reactions of the organic precursors (Fig. 2d).[12]

Bulk passivation with $PbCl_2$: four perovskite precursors in one source

To further improve the perovskite thin-film quality and by taking advantage of the single-source nature of our PLD process, we introduce $PbCl_2$ in the target, now containing MAI: FAI: PbI_2: $PbCl_2$, with MAI/FAI molar ratios of 0.75/0.25, and partially substituting PbI_2 by molar amount for 10, 20, 30 and 50 mol% of $PbCl_2$, respectively (Supplementary Fig. 2). The chosen amount of $PbCl_2$ incorporation in the target is based on prior investigations in co-evaporated MHPs.[20] Fig. 3a displays the specular XRD patterns of thin films grown from targets containing $PbCl_2$ at molar ratios ranging from 0 mol% to 30 mol%. Notably, a subtle shift in the lattice is observed with increasing the Cl^--source content and a preferential (100) plane orientation is evident in all samples.[28] Several articles have reported limited incorporation of Cl^- precursors into the lattice of iodide-based perovskites, typically on the order of 3-4%.[29] This limited incorporation is attributed to the energetically unfavorable nature of Cl^- integration, owing to the significant difference in the ionic radii between Cl^- and I^- ions (contrary to mixtures where Br^- ions are present).[30] A slower conversion to the perovskite phase in the presence of Cl^- may explain the behavior observed in the 50 mol% $PbCl_2$ source case, where, despite using the same number of laser pulses for thin film growth, a much thinner and partially converted perovskite film was obtained (Supplementary Fig. 3).[31] Consequently, for the subsequent analysis, we excluded the 50 mol% $PbCl_2$ source. Notably, no diffraction signals were observed in any thin film corresponding to the formation of other perovskite phases, $MAPbCl_3$ or $FAPbCl_3$, typically expected at 15-16 2theta.[32]

Fig. 3b displays the normalized PL spectra for the PLD-grown thin films. A slight redshift in the bandgap when employing Cl^- sources does not correspond with Cl^- incorporation in the lattice, which is expected to cause a blueshift of the bandgap.[32] Further, this slight redshift is consistently observed in all samples from sources with Cl^-, suggesting a distinct growth behavior or strain induced by the influence of $PbCl_2$ during the thin film growth, as also previously noted by Yalcinkaya *et al.*[33] Other reports have similarly indicated that the absorption edge in samples containing Cl^-, either in the precursor solution or introduced during post-treatment were approximately the same as the control samples.[29,34,35] Fig. 3c presents the calculated Urbach energy (E_U) extracted from the PL data. For all investigated thin films,

E_U values remained below 15 meV, indicating good optoelectronic performance for all the thin films grown on 2PACz.[36] Samples originating from the 20 mol% $PbCl_2$ source exhibit a 1.8 meV lower E_U compared to samples without $PbCl_2$; this difference arguably explains the gain of 23 mV in the V_{OC} of finalized solar cells using this composition.[37]

To investigate the thin-film surface composition and the potential presence of Cl^-, we conducted XPS measurements. The survey scan of all samples is provided in Supplementary Fig. 4, while a closer examination of the Cl 2p core level region is presented in Fig. 3d. No discernible Cl^- peaks were detected in any of the samples, irrespective of the Cl^- content of the source. This finding is in line with observations made in previous studies where passivation or post-treatments involving Cl^- precursors led to observable changes in morphology, microstructure, and performance yet did not yield detectable Cl^- on the thin film surface.[34,35,38–42] It is worth noting that the presence of Cl^- has been reported by other studies using XPS.[20,21] However, in those cases, other phases, such as $CsPbCl_3$ or $MAPbCl_3$, are also present, as confirmed by XRD analysis. This coexistence of phases complicates the interpretation as to whether the Cl^- is incorporated in the lattice or as a segregated phase.[43] Given this complexity, a more detailed analysis, for instance by employing ^{207}Pb NMR, should be followed to discriminate contributions from the Pb-Cl ionic bonds connectivity in a mixed-halide perovskite or a segregated phase.[44] Cross-sectional elemental mapping via scanning transmission electron microscopy/energy dispersive X-ray spectroscopy (STEM-EDS) did not detect the presence of Cl^- within the bulk of the thin films either (Supplementary Fig. 5). This outcome contrasts with the results reported by Lee *et al.*[45]; nevertheless, their films also exhibited the presence of $MAPbCl_3$ as confirmed by XRD analysis. Wang *et al.* conducted SEM-EDS on CsFA-based thin film fabricated with $PbCl_2$ and similarly did not detect Cl^-.[35] One possible explanation for the absence of detectable Cl^- in the bulk of any PLD-grown thin films is the release of Cl^- in the form of MACl or FACl, either during the growth process or upon annealing of perovskite film at 100 °C for 10 minutes.[40–43,46,47]

Additionally, the XPS analysis of the Pb 4f core levels demonstrates no significant variations attributable to potential chemical states between Pb-I and Pb-Cl, except for the presence of metallic lead (Pb^0) in the samples from the 0 and 10 mol% $PbCl_2$ sources (Fig. 3e). These observations indicate superior stability and reduction of deep defect states in samples grown from the 20 and 30 mol% $PbCl_2$ sources.[48,49] Analysis of the N 1s core levels reveals minor changes in the cation ratio MA^+: FA^+, even when the PLD sources contain the same MA^+: FA^+ cation ratio, suggesting that the use of Cl^- could modify the growth as well as the cation ratio incorporated in the final thin films (Fig. 3f).[31] Nevertheless, there is no clear trend regarding the cation ratio varying from 52-56 mol% FA^+ (Fig. 3g). Furthermore, an analysis of the I/Pb ratio implies a significant iodine deficiency for the films from the 0 mol% $PbCl_2$ (I/Pb of 2.50) and less iodide-deficient samples with increasing Cl^- content in the PLD source in comparison to a reference

pressed powder of $MA_{0.50}FA_{0.50}PbI_3$ (I/Pb of 2.94). These outcomes reveal a potentially more uniform and less defective growth mode of the MHP materials by PLD when Cl^- is present in the source.[28,42,49]

In addition, Fig. 3h displays the films grown from a PLD source which contains 20 mol% $PbCl_2$, showing a compact void-free structure and, thus, an improved morphology compared to the control samples (Fig. 1e). Despite conducting surface and bulk chemical compositional analysis, no evidence of Cl^- was detected either at the surface or in the bulk of the thin films; however, evident morphological, structural, optical, and compositional alterations provide valuable insights into the impact of Cl^- during the thin-film growth process. From now on the nomenclatures $MA_{1-x}FA_xPbI_3(Cl)_y$ and $MA_{1-x}FA_xPbI_3$ are employed to identify samples grown from PLD sources with and without $PbCl_2$

Surface passivation via post-treatment: *in-situ* PL monitoring

Next, surface passivation on the PLD-grown perovskites films was tested. The procedure for 2D passivation, reported previously by Azmi *et al.*[22], was followed, where the 2D layered perovskites are formed by surface treatment of the 3D perovskite with OAmI ligands in chloroform (CF). This 2D layer not only could effectively reduce surface recombination but also contribute to enhancing the PSC stability. The successful 2D layer formation on the PLD-grown perovskites and the effect on the optoelectronic quality were followed via *in-situ* PL and confirmed by *ex-situ* PL.[50] Supplementary Fig 6.a displays the linear increase of the QFLS with excitation of passivated $MA_{1-x}FA_xPbI_3$ and $MA_{1-x}FA_xPbI_3(Cl)_y$ thin films at different sun intensities.[51] The slope of the QFLS is shown in Supplementary Fig 6.b, where $MA_{1-x}FA_xPbI_3(Cl)_y$ thin films deposited from a 20 mol% $PbCl_2$ source exhibit superior radiative efficiencies. Thus, better solar cell performance is expected to be obtained from these films than from those grown with the 0 or 30 mol% $PbCl_2$ target. Note that these measurements are done on films grown on glass, which differs from QFLS measurements performed on complete devices.

Fig 4 a-c. displays the evolution of the PL emission of $MA_{1-x}FA_xPbI_3(Cl)_y$ thin film deposited from a 20 mol% $PbCl_2$ measured *in-situ* at the different passivation stages. Before the passivation, we tracked the PL response of the thin film for 300 s (Fig 4d.). During this time, we observed a gradual decrease in the PL intensity of the 3D perovskite, which increased again immediately after the application of OAmI at RT. The samples were kept inside the spin coater for 540 more seconds to track the evolution of the 2D phase at RT post-spin-coating. During the first ~180 seconds (60 seconds of spinning + 120 seconds post-spinning), the PL emission comes only from the 3D perovskite, but approximately 200 seconds after the RT application of OAmI by spin coating, the n = 1 formation of the 2D-layered perovskite is observed (Fig 4e.). Subsequent to spin coating, the samples were annealed at 100 ^oC for 10 min (Fig 4f.). During the annealing, PL emission from n = 2 and n = 1 phases are immediately observed. This demonstrates that 2D-OAmI-based layered perovskites can be formed on the top surface of PLD-grown samples and the influence of temperature in promoting the n = 1 or n = 2 layered formation.

P–i–n solar cells with PLD-grown MHP and 2D passivation

To elucidate the role of Cl^- on the solar cell performance, we first fabricated *p–i–n* solar cells with the configuration ITO/2PACz/PLD-$MA_{1-x}FA_xPbI_3(Cl)_y/C_{60}$/BCP/Ag. Fig 5. a displays the J-V curve characteristics of the champion solar cell containing PLD-grown $MA_{1-x}FA_xPbI_3$ and $MA_{1-x}FA_xPbI_3(Cl)_y$ from 0 and 20 mol% $PbCl_2$ sources, respectively. The control solar cells $MA_{1-x}FA_xPbI_3$ resulted in modest performance above 14% with a critical V_{OC} deficit, suggesting significant non-radiative recombination losses. Interestingly, the solar cells with $MA_{1-x}FA_xPbI_3(Cl)_y$ exhibited an improved FF with slightly higher V_{OC}, reflected in an almost 1% absolute gain in the PCE (the FF and V_{OC} values are summarized in Table S2 of Supplementary information). This is expected as the samples from the 20 mol% $PbCl_2$ source showed higher radiative efficiency, higher E_U, less surface defects (no metallic lead following XPS), and a void-free morphology, which helps suppress non-radiative recombination losses.[48] Still, the V_{OC} deficit and the iodide deficiency identified through XPS analysis indicate the possibility of defective surfaces arising from iodine vacancies. Due to their low migration energy, such vacancies are one of the most common surface defect types in halide perovskite absorbers.[15]

Secondly, we passivate the surface of the PLD-grown MHP films deposited from 0 and 20 mol% $PbCl_2$ sources by employing a dilute OAmI solution in CF, applied at RT (2D formation mostly n = 1), without any further post-treatment with the configuration ITO/2PACz/PLD-$MA_{1-x}FA_xPbI_3(Cl)_y$ /2D-OAmI/C_{60}/BCP/Ag. Fig 5.a reveals a remarkable improvement primarily evident in the V_{OC} by effectively reducing non-radiative recombination centers. Further, passivated samples from a 20 mol% $PbCl_2$ source exhibit 21 mV higher V_{OC} than those from a 0 mol% $PbCl_2$ source, as predicted by E_U analysis. This higher V_{OC} is also in agreement with the obtained QFLS in Supplementary Fig 6.a for the passivated PLD-grown perovskite samples on glass.

Consequently, a substantial increase in the device PCE, up to 19.7% for our champion device, is obtained. The statistical analysis of the J-V characteristic in Fig 5.b shows an overall improvement in all photovoltaic parameters for $MA_{1-x}FA_xPbI_3(Cl)_y$ /2D solar cells. Fig 5.c displays the EQE plot where the short-circuit current (J_{SC}) obtained by integration under the curve corresponds with the J_{SC} extracted from the J-V curves of the 2D passivated samples. Fig 5.d compares the QFLS of the average devices. An evident mismatch between the QFLS and the measured V_{OC} for the samples grown with $PbCl_2$ suggests that the interface formation between the perovskite/C_{60} also introduces non-radiative recombination centers that are decreased when introducing a 2D interface between perovskite/C_{60}. This proves that the synergy between bulk and surface passivation strategies effectively suppresses non-radiative recombination losses.

Device stability and state-of-the-art PCE of single-source vapor deposited MHP solar cells

A further analysis evaluating the stability of devices featuring PLD-grown absorbers is shown in Fig 6.a where devices incorporating top-contact 2D passivation on $MA_{1-x}FA_xPbI_3(Cl)_y$ films with 20 mol% of $PbCl_2$ retain 85% PCE after 1000 h at 85 °C. In contrast, the devices based on solution spin-coated

processed with identical passivation conditions only retain ~72% PCE. Further, the examination of the maximum power point (MPP) tracking in Fig 6.b reveals that these devices maintain ~88% of their initial PCE after 90 h. Here, the synergistic benefits derived from incorporating Cl^- ions during the PLD-growth process, followed by the 2D-surface passivation, demonstrate a promising path toward designing and fabricating more robust devices. Finally, Fig 6.c visually represents the-state-of-the-art single-source vapor deposition methods used to prepare different halide perovskite compositions, along with the reported solar cell efficiency. To our knowledge, this study represents the highest performance of a solar cell containing a MHP absorber grown by a single-source vapor deposition method, specifically PLD. Supplementary Table 3 provides the corresponding reference of each method.

Outlook

PLD is a promising route for depositing multi-compound halide perovskite materials from a single source. The control over the target composition and confined transfer of precursors allows for overcoming the volatility challenges of single-source vapor deposition methods for MHP, bridging the gap between the benefits of vapor phase deposition methods and the challenges of stoichiometric control from multiple precursors. Bulk passivation of thin films by adding $PbCl_2$ as a fourth precursor to the single target is demonstrated. $PbCl_2$ addition resulted in less defective and more stable $MA_xFA_{1-x}PbI_3(Cl)_y$ films with a void-free morphology. Furthermore, by combining the synergy between bulk and surface passivation strategies using 2D-layered perovskites, we obtained promising PCE above 19% with improved stability. This work highlights the importance of exploring and innovating vapor phase deposition methods, in this case, demonstrating the possibility of fabricating efficient perovskite devices with complex compositions and from a single target in a single-step process. Moreover, the work highlights the significance of exploring diverse bulk and surface passivation strategies related to the type of defects or recombination centers that must be diminished in vapor-deposited perovskites. Further, the potential of PLD to grow halide perovskite absorbers of tunable compositions via a single source paves the way for exploring other perovskite compositions with more suitable bandgaps for tandem solar cells where thickness control and conformality are paramount.

Methods

PLD targets. Methylammonium iodide (MAI, > 99.99% greatcell solar), formamidinium iodide (FAI, > 99.99% greatcell solar), lead iodide (PbI_2, 99.999% Sigma-Aldrich), and lead chloride ($PbCl_2$, ultra-dry, 99,999%, Alfa Aesar) powders were weighted (analytical balance, ± 0.01 mg) inside an N_2 filled glovebox. Non-stoichiometric ratios of the inorganic to the organic components (PbI_2/$PbCl_2$: MAI/FAI = 1:8) were used as determined in previous work.[11] The mol ratio of the organic components MAI: FAI was chosen as 75:25 as optimized in a previous work.[12] The $PbCl_2$ content in the target was varied from 0-50 mol% with respect to PbI_2. Target 0, 10, 20, 30 and 50 mol% $PbCl_2$, (PbI_2 : $PbCl_2$: MAI : FAI) = (1.5: 0 : 8·1.5·0.75 : 8·1.5·0.25), (1.35: 0.15 : 8·1.5·0.75 : 8·1.5·0.25), (1.2: 0.3 : 8·1.5·0.75 : 8·1.5·0.25), (1.05: 0.45 : 8·1.5·0.75 : 8·1.5·0.25), (0.75: 0.75 : 8·1.5·0.75 : 8·1.5·0.25), respectively (given in mol units). The powder precursors,

as received, were transferred to zirconia-coated vials containing zirconia beds and mixed using a house-built rotatory ball miller. Subsequently, the mixed powders were uniaxially pressed at RT, employing 470 MPa into a ≈ 2.5 mm thick disc of 20 mm in diameter. Before each deposition the PLD targets are pre-ablated. After each deposition the target surface is polished with sandpaper to expose fresh material.

Pulsed Laser Deposition (PLD). PLD was performed using a Coherent KrF excimer laser (λ = 248 nm) guided via a series of aligned mirrors and lenses to ablate the solid target inside a customized (TSST Demcon) vacuum chamber (base pressure ~1.0 x 10^{-7} mbar) in an Ar atmosphere (working pressures: 0.02 mbar). The single-source halide perovskite material, synthesized via mechanochemical methods, is set in rotation, creating a circular ablation pattern. Multiple depositions from a single target were performed on a “fresh” ground area of the target. A target-to-substrate distance of 55 mm was kept constant for all the depositions. All depositions took place at ≈ 40 °C (resistive heater set point). Based on previously optimized conditions, the laser fluence was kept constant at 0.31 J cm^{-2}. An apparent (local) frequency of 4 Hz, 18000 pulses (corresponding to 18 scans ≈ 400 nm-thick films), and a spot size of 2.33 mm^2 were used for all samples. All depositions were performed with a sample stage scanning squared pattern of 36 x 36 mm^2 at a speed of 2 mm/s, ensuring homogeneous coverage on a 2.54 cm^2 area. By controlling the number of laser pulses, thin films of varying thicknesses can be obtained. For the optimized 400 nm thin films in a 2.54 cm^2 area, the deposition rate is approximately 1 Å/s (6 nm/min). For GIWAXS measurements, the sample area was 1$cm^{2,}$ and the scanning pattern was 30 x 30 mm^2 at a speed of 2 mm/s. The same number of scans (18) is required to grow 400 nm films.

X-ray diffraction (XRD). Thin film measurements were done in air (~ 40 % humidity, 22 °C) in a symmetric configuration using a PANalytical X’Pert PRO with a Cu anode X-ray source.

Grazing-incidence wide-angle X-ray scattering (GIWAXS) measurements. GIWAXS data were collected at the DESY synchrotron in Hamburg, Germany, at the microfocus and nanofocus X-ray scattering beamline P03 of PETRA III.[52] A Lambda9M detector (X-Spectrum) with a pixel size of 55 × 55 m was used to collect wide-angle scattering data. The sample-to-detector distance was 212 mm as determined from a LaB_6 capillary calibration, and an incident angle of 0.4° was used. An X-ray wavelength of 1.048 Å was used. For depth-dependent measurements, the incident angle varied between 0.05 and 0.4°. Data analysis, including the transformation to reciprocal space, was done with the software package INSIGHT.[53] The data was indexed with a cubic perovskite structure (space group 221, a=b=c=6.275 Å).

Photoluminescence (PL). Measurements were done in air (~ 40 % humidity, 22 °C) in a home-built setup consisting of a 520 nm laser Diode Module, 100 mW (Matchbox series), and a StellarNetBLUE-Wave Spectrometer coupled with a fiber optic. The *in-situ* PL measurements were carried out in an N_2-filled glovebox using a home-built setup. Excitation was performed using a 405 nm laser diode, and the PL emission was collected via a fiber-coupled Ocean Insight spectrometer (QEpro). Before applying the 2D passivation, the samples were kept on the spin coater stage (without spinning) while measuring the *in-situ* PL emission from the 3D perovskites for 5 minutes. Subsequently, a 2-step spinning was employed

(3000 rpm for 10 s and 5000 rpm for 20 s). The 2D passivation (2.5 mg of OAmI in 1 mL CF) was applied during the first 5s of the slow step. After the spinning the samples were kept 9 more minutes inside the spin coater to track the evolution of the 2D phase at RT.

X-Ray Photoelectron Spectroscopy (XPS). Measurements were performed using an Omicron XM 1000 Al Kα monochromated X-ray source (1486.6 eV, FWHM = 0.26 eV) and an Omicron EA 125 energy analyzer with a pass energy of 50 eV at a photoemission angle 45°. An electron neutralizer beam is used to minimize binding energy shifts. During measurements, the pressure was < 2×10^{-10} mbar. The samples were fixed with a copper double-sided conductive adhesive tape and analyzed as loaded. The spectra' peak positions and width were fitted using a Gaussian–Lorentzian function (GL). A Shirley background was employed using the CasaXPS Software. During the fitting, only constraints of the FWHM were employed. The binding energy of the adventitious carbon, C-(C, H), was set at 285 to adjust the binding energy scale of all spectra.

Scanning Electron SEM Images: Secondary Electron SEM Images were acquired with acceleration voltages ranging from 0.75 to 1.5 kV using a Zeiss MERLIN HR-SEM.

Transmission electron microscopy (TEM) and focused ion beam (FIB). For the (Scanning) Transmission Electron Microscopy (S/TEM)-based study, we meticulously prepared a cross-sectional electron-transparent lamella using a focused ion beam (FIB) within the Scanning Electron Microscope (SEM-FIB Helios G5 DualBeam, FEI). STEM experiments were performed using the Cs-probe-corrected ThermoFisher Titan 60-300 Cubed TEM, equipped with a Four-Quadrant SuperX Energy Dispersive Spectrometry (EDS) Detector for elemental mapping (STEM-EDS). The acquired TEM data were analyzed using specialized software packages, including Gatan™ Digital Micrograph and Thermo Scientific™ Velox suites.

Single junction solar cell fabrication. ITO glass substrates (2.54 × 2.54 mm, 15 Ω/sq, XinYan TechnologyLTD were cleaned in ultrasonic baths of 2 v/v % solution of Hellmanex III, deionized water, acetone, and 2-propanol for 10 min each, followed by a 15 min UV-Ozone treatment. 100 uL of self-assemble monolayers ([2-(9H-carbazol-9-yl)ethyl]phosphonic acid (2PACz), TCI , 1 mg/mL in Ethanol) were statically deposited on ITO (10 s waiting time), followed by a spin coating step at 5000 rpm for 30 s. The ITO/2PACz substrates were annealed at 100 °C for 10 min, followed by a washing step, 100 µL Ethanol. Subsequently, the substrate was loaded in the PLD chamber for the deposition of the MHP absorber described above. The samples were subsequently shipped in an inert atmosphere to proceed with the passivation steps at KAUST (waiting time ~ 7 days). Before the OAIm passivation, all samples were annealed at 100 °C for 10 min in an N_2-filled Glovebox. OAIm was applied as described in a previous work following the RT approach.[22] Successively, 25 nm of C_{60}, 5 nm of BCP, and 120 nm of Ag were evaporated at deposition rates of 0.2, 0,1, and 2 Å/s , respectively. 120 nm MgF_2 was deposited at the glass side. The device area is defined by an aperture masked 0.0633 cm^2.

Device characterization: The device *J-V* characteristics were measured in the N_2-filled glovebox under artificial sunlight calibrated to AM 1.5 G (100 mW cm^{-2}) using Abet Technologies Sun 3000 Solar

Simulator integrated with Keithley 2400 source unit. The light source was calibrated to a KG-5 filtered-covered mono-silicon standard cell (Newport). Both forward scan (J_{SC} to V_{OC}, -0.1 à 1.2 V) and reverse scan (V_{OC} and J_{SC}, 1.2 à -0.1 V) were applied to all devices with 50 mV s^{-1} scan rate without any treatment before the measurement. The external quantum efficiency (EQE) spectra were measured using a 400 W Xenon lamp equipped with a monochromator and filter, calibrated to 603621 Silicon and Germanium Reference detector, all samples with antireflecting MgF_2 coating.

Stability test: The thermal stability test was performed by placing the non-encapsulated cells on a hot plate at 85 °C in an N_2-filled glovebox. The devices were measured periodically until 1000 hours. The operational stability tests were carried out at the MPPT under 1-sun illumination at a temperature of ~40 °C. The voltage at the MPPT was automatically applied, and the power output of the devices was tracked for around 90 hours.

QFLS: Perovskite films were deposited on a patterned ITO substrate. The hyperspectral imaging system (Photon, etc., IMA) integrated into a microscope with 20X magnification and 2 nm spectral resolution was used to collect the PL spectra. The signal was collected after exciting the sample with a 532 nm laser, which was calibrated to 1 sun condition by adjusting the power density. The absolute intensity calibration procedure of the setup was reported earlier.[54] The QFLS was calculated using home-built MATLAB code following the previous experiment by using PL spectra and absorption coefficient.[55]

Declarations

Competing interests: The authors declare no competing interests.

Data availability

All data generated or analyzed during this study are included in the published article and its Supplementary Information and Source Data. Source data are provided in this paper.

Acknowledgements

This work is funded by the European Research Council (ERC) under the European Union's Horizon 2020 Research and Innovation Program (CREATE, Grant Agreement No. 852722). The authors thank Dominic Post and Jeroen van Valkenhoef for the technical support with the experiments, TSST Demcon for the PLD experimental support, Raphael Moral for help regarding *in-situ* PL measurements and 2D passivation discussions, Mark Smithers for the SEM images, and Vojta Kliner for the support during the PLD sample preparation. Work at the Molecular Foundry was supported by the Office of Science, Office of Basic Energy Science, of the U.S. Department of Energy under Contract No. DE-AC02-05CH1123. D.-K.L. acknowledge Office of Science, Office of Basic Energy Sciences, of the U.S. Department of Energy under contract number DE-SC-0023355.

Authors and Affiliations

MESA+ Institute for Nanotechnology, University of Twente, The Netherlands: Tatiana Soto-Montero, Suzana Kralj, Junia S. Solomon, Daniel M. Cunha, Wiria Soltanpoor, and Monica Morales-Masis.

Physical Sciences and Engineering Division, KAUST Solar Center, King Abdullah University of Science and Technology (KAUST): Randi Azmi, Drajad Satrio Utomo, Esma Ugur, Badri Vishal,Erkan Aydin, and Stefaan De Wolf.

Technical University of Munich, TUM School of Natural Sciences, Department of Physics, Germany: Manuel Reus and Peter Müller-Buschbaum.

Technical University of Munich, Heinz Maier-Leibnitz-Zentrum (MLZ), Germany: Peter Müller-Buschbaum.

Institute of Physics, Academy of Science of the Czech Republic: Martin Ledinsky

Chemical Science Division, Liquid Sunlight Alliance (LiSA), Lawrence Berkeley National Laboratory, United States: Finn Babbe

Molecular Foundry Division, Lawrence Berkeley National Laboratory, California, United States: Do Kyoung Lee and Carolin M. Sutter-Fella.

Contribution

T.S-M and M.M-M conceived the idea, designed the experiments, development of PLD-grown MHP, wrote the paper, and prepared the figures. S.K and J.S.S, contributed to the development of the PLD-grown MHP, T.S-M and S.K carried out device fabrication. R.A and D.S.U contributed to device fabrication and stability test. E.U, D.S.U and R.A contributed to the PSCs QFLS calculation. W.S contributed to the PSCs baseline. M.R and P.M-B contributed to the GIWAXS data acquisition and analysis. M.M.M, T.S-M, W.S, S.K, J.S.S, D.M.C, M.L, E.A, S.D.W, E.U, D.S.U and R.A carried out data analysis. D.M.C contributed to the python codes and to PLD technical support. D.-K.L and C.S-F contributed to the *in-situ* PL measurements and data analysis. F.B contributed to the QFLS data acquisition and analysis. B.V performed the FIB and STEM characterization. E.A, S.D.W, C.S-F and M.M-M, supervised different parts of the work., and all authors commented on the manuscript.

References

1. Leijtens, T., Bush, K. A., Prasanna, R. & McGehee, M. D. Opportunities and challenges for tandem solar cells using metal halide perovskite semiconductors. Nat. Energy 3, 828–838 (2018).
2. Ávila, J., Momblona, C., Boix, P. P., Sessolo, M. & Bolink, H. J. Vapor-Deposited Perovskites: The Route to High-Performance Solar Cell Production? *Joule* 1, 431–442 (2017).
3. Saliba, M. *et al.* Cesium-containing Triple Cation Perovskite Solar Cells: Improved Stability, Reproducibility and High Efficiency. Energy Environ. Sci. 9, 1989–1997 (2016).

4. Igual-Muñoz, A. M., Ávila, J., Boix, P. P. & Bolink, H. J. $FAPb_{0.5}Sn_{0.5}I_3$: A Narrow Bandgap Perovskite Synthesized through Evaporation Methods for Solar Cell Applications. Sol. RRL 4, 1900283 (2020).
5. Gil-Escrig, L. *et al.* Efficient Wide-Bandgap Mixed-Cation and Mixed-Halide Perovskite Solar Cells by Vacuum Deposition. ACS Energy Lett. 6, 827–836 (2021).
6. Soltanpoor, W. *et al.* Hybrid Vapor-Solution Sequentially Deposited Mixed-Halide Perovskite Solar Cells. ACS Appl. Energy Mater. 3, 8257–8265 (2020).
7. Ojeda-G-P, A., Döbeli, M. & Lippert, T. Influence of Plume Properties on Thin Film Composition in Pulsed Laser Deposition. Adv. Mater. Interfaces 5, 1–16 (2018).
8. Rodkey, N. *et al.* Pulsed Laser Deposition of $Cs_2AgBiBr_6$: from mechanosynthesized powders to dry, single-step deposition. Chem. Mater. 33, 7417–7422 (2021).
9. Sebastiá-Luna, P. *et al.* Chalcohalide Antiperovskite Thin Films with Visible Light Absorption and High Charge-Carrier Mobility Processed by Solvent-Free and Low-Temperature Methods. Chem. Mater. 35, 6482–6490 (2023).
10. Kiyek, V. M. *et al.* Single-Source, Solvent-Free, Room Temperature Deposition of Black γ-$CsSnI_3$ Films. Adv. Mater. Interfaces 7, 1–5 (2020).
11. Soto-Montero, T. *et al.* Single-Source Pulsed Laser Deposition of $MAPbI_3$. 2021 *IEEE 48th Photovolt. Spec. Conf.* 1318–1323 (2021).
12. Soto-Montero, T. *et al.* Single-Source Vapor-Deposition of $MA_{1-x}FA_xPbI_3$ Perovskite Absorbers for Solar Cells. Adv. Funct. Mater. 2300588 (2023) doi:10.1002/adfm.202300588.
13. Smirnov, Y. *et al.* Wafer-scale pulsed laser deposition of ITO for solar cells: Reduced damage vs. interfacial resistance. Mater. Adv. 3, 3469–3478 (2022).
14. Zanoni, K. P. S. *et al.* Tin(IV) Oxide Electron Transport Layer via Industrial-Scale Pulsed Laser Deposition for Planar Perovskite Solar Cells. ACS Appl. Mater. Interfaces 15, 32621–32628 (2023).
15. Luo, D., Su, R., Zhang, W., Gong, Q. & Zhu, R. Minimizing non-radiative recombination losses in perovskite solar cells. Nat. Rev. Mater. 5, 44–60 (2020).
16. Jariwala, S. *et al.* Local Crystal Misorientation Influences Non-radiative Recombination in Halide Perovskites. Joule 3, 3048–3060 (2019).
17. Byranvand, M. M. & Saliba, M. Defect Passivation of Perovskite Films for Highly Efficient and Stable Solar Cells. Sol. RRL 5, (2021).
18. Chiang, Y. *et al.* Vacuum-Deposited Wide-Bandgap Perovskite for All-Perovskite Tandem Solar Cells. ACS Energy Lett. 8, 2728–2737 (2023).
19. Al-Ashouri, A. *et al.* Conformal monolayer contacts with lossless interfaces for perovskite single junction and monolithic tandem solar cells. Energy Environ. Sci. 12, 3356–3369 (2019).
20. Lohmann, K. B. *et al.* Solvent-Free Method for Defect Reduction and Improved Performance of p-i-n Vapor-Deposited Perovskite Solar Cells. ACS Energy Lett. 7, 1903–1911 (2022).
21. Babaei, A. *et al.* Preparation and Characterization of Mixed Halide $MAPbI_{3-x}Cl_x$ Perovskite Thin Films by Three-Source Vacuum Deposition. Energy Technol. 8, 1–5 (2020).

22. Azmi, R. *et al.* Damp heat – stable perovskite solar cells with tailored-dimensionality 2D/3D heterojunctions. Science (80-.). 5784, 1–9 (2022).
23. Shepelin, N. A. *et al.* A practical guide to pulsed laser deposition. Chem. Soc. Rev. 52, 2294–2321 (2023).
24. Palazon, F., El Ajjouri, Y. & Bolink, H. J. Making by Grinding: Mechanochemistry Boosts the Development of Halide Perovskites and Other Multinary Metal Halides. Adv. Energy Mater. 10, 1–13 (2020).
25. Guesnay, Q., Sahli, F., Ballif, C. & Jeangros, Q. Vapor deposition of metal halide perovskite thin films: Process control strategies to shape layer properties. APL Mater. 9, (2021).
26. Abzieher, T. *et al.* From Groundwork to Efficient Solar Cells: On the Importance of the Substrate Material in Co-Evaporated Perovskite Solar Cells. Adv. Funct. Mater. 31, (2021).
27. Dosch, H., Batterman, B. W. & Wack, D. C. Depth-controlled grazing-incidence diffraction of synchrotron x radiation. Phys. Rev. Lett. 56, 1144–1147 (1986).
28. Barrows, A. T. *et al.* Monitoring the Formation of a $CH_3NH_3PbI_{3-x}Cl_x$ Perovskite during Thermal Annealing Using X-Ray Scattering. Adv. Funct. Mater. 26, 4934–4942 (2016).
29. Colella, S. *et al.* $MAPbI_{3-x}Cl_x$ Mixed Halide Perovskite for Hybrid Solar Cells: The Role of Chloride as Dopant on the Transport and Structural Properties. Chem. Mater. 25, 4613–4618 (2013).
30. Yoon, S. J., Stamplecoskie, K. G. & Kamat, P. V. How Lead Halide Complex Chemistry Dictates the Composition of Mixed Halide Perovskites. J. Phys. Chem. Lett. 7, 1368–1373 (2016).
31. Song, T. Bin *et al.* Revealing the Dynamics of Hybrid Metal Halide Perovskite Formation via Multimodal In Situ Probes. Adv. Funct. Mater. 30, 1–11 (2020).
32. Caputo, M. *et al.* Electronic structure of $MAPbI_3$ and $MAPbCl_3$: importance of band alignment. Sci. Rep. 9, 1–11 (2019).
33. Yalcinkaya, Y. *et al.* Chemical Strain Engineering of $MAPbI_3$ Perovskite Films. Adv. Energy Mater. 12, (2022).
34. Ren, A. *et al.* Efficient Perovskite Solar Modules with Minimized Nonradiative Recombination and Local Carrier Transport Losses. Joule 4, 1263–1277 (2020).
35. Wang, S. *et al.* Over 24% efficient MA-free $Cs_xFA_{1-x}PbX_3$ perovskite solar cells. Joule 6, 1344–1356 (2022).
36. Ugur, E. *et al.* Life on the Urbach Edge. J. Phys. Chem. Lett. 13, 7702–7711 (2022).
37. Ledinsky, M. *et al.* Impact of cation multiplicity on halide perovskite defect densities and solar cell voltages. J. Phys. Chem. C 124, 27333–27339 (2020).
38. Philippe, B. *et al.* Chemical and Electronic Structure Characterization of Lead Halide Perovskites and Stability Behavior under Different Exposures - a Photoelectron Spectroscopy Investigation. Chem. Mater. (2015).
39. Kim, T. G., Seo, S. W., Kwon, H., Hahn, J. & Kim, J. W. Influence of halide precursor type and its composition on the electronic properties of vacuum deposited perovskite films.

Phys.Chem.Chem.Phys., 17, 24342–24348 (2015).

40. Kim, M. *et al.* Methylammonium Chloride Induces Intermediate Phase Stabilization for Efficient Perovskite Solar Cells. Joule 3, 2179–2192 (2019).
41. Yu, H. *et al.* The role of chlorine in the formation process of '$CH_3NH_3PbI_{3-x}Cl_x$' perovskite. Adv. Funct. Mater. 24, 7102–7108 (2014).
42. Stone, K. H. *et al.* Transformation from crystalline precursor to perovskite in $PbCl_2$-derived $MAPbI_3$. Nat. Commun. 9, (2018).
43. Ono, L. K., Leyden, M. R., Wang, S. & Qi, Y. Organometal halide perovskite thin films and solar cells by vapor deposition. J. Mater. Chem. A 4, 6693–6713 (2016).
44. Karmakar, A. *et al.* Mechanochemical Synthesis of Methylammonium Lead Mixed-Halide Perovskites: Unraveling the Solid-Solution Behavior Using Solid-State NMR. Chem. Mater. 30, 2309–2321 (2018).
45. Lee, M. M., Teuscher, J., Miyasaka, T., Murakami, T. N. & Snaith, H. J. Efficient Hybrid Solar Cells Based on Meso-Superstructured Organometal Halide Perovskites. Science (80-.). 338, 643–647 (2012).
46. Sun, Y., Chen, H., Zhang, T. & Wang, D. Chemical state of chlorine in perovskite solar cell and its effect on the photovoltaic performance. J. Mater. Sci. 53, 13976–13986 (2018).
47. Kang, D. H., Lee, S. U. & Park, N. G. Effect of Residual Chloride in $FAPbI_3$ Film on Photovoltaic Performance and Stability of Perovskite Solar Cell. ACS Energy Lett. 8, 2122–2129 (2023).
48. Liang, J. *et al.* Origins and influences of metallic lead in perovskite solar cells Origins and influences. Joule 6, 816–833 (2022).
49. Shen, X. *et al.* Chloride-Based Additive Engineering for Efficient and Stable Wide-Bandgap Perovskite Solar Cells. Adv. Mater. 2211742, 1–11 (2023).
50. Guaita, M. G. D. *et al.* Influence of Methylammonium Chloride on Wide-Bandgap Halide Perovskites Films for Solar Cells. Adv. Funct. Mater. (2023) doi:10.1002/adfm.202307104.
51. Babbe, F., Choubrac, L. & Siebentritt, S. The Optical Diode Ideality Factor Enables Fast Screening of Semiconductors for Solar Cells. Sol. RRL 2, 1–6 (2018).
52. Buffet, A. *et al.* P03, the microfocus and nanofocus X-ray scattering (MiNaXS) beamline of the PETRA III storage ring: The microfocus endstation. J. Synchrotron Radiat. 19, 647–653 (2012).
53. M. A. Reus, Reb, L. K. & Müller-Buschbaum, P. The in situ GIXS heuristic tool for efficient reduction of grazingincidence scattering data. https://www.ph.nat.tum.de/functmat/%0Aforschung/insight/ (accessed: April 2023). (2023).
54. Delamarre, A., Lombez, L. & Jean-Francois, G. Characterization of solar cells using electroluminescence and photoluminescence hyperspectral images. J. Photonics Energy 2, 027004 (2012).
55. Aydin, E. *et al.* Ligand-bridged charge extraction and enhanced quantum efficiency enable efficient n-i-p perovskite/silicon tandem solar cells. Energy Environ. Sci. 14, 4377–4390 (2021).

Figures

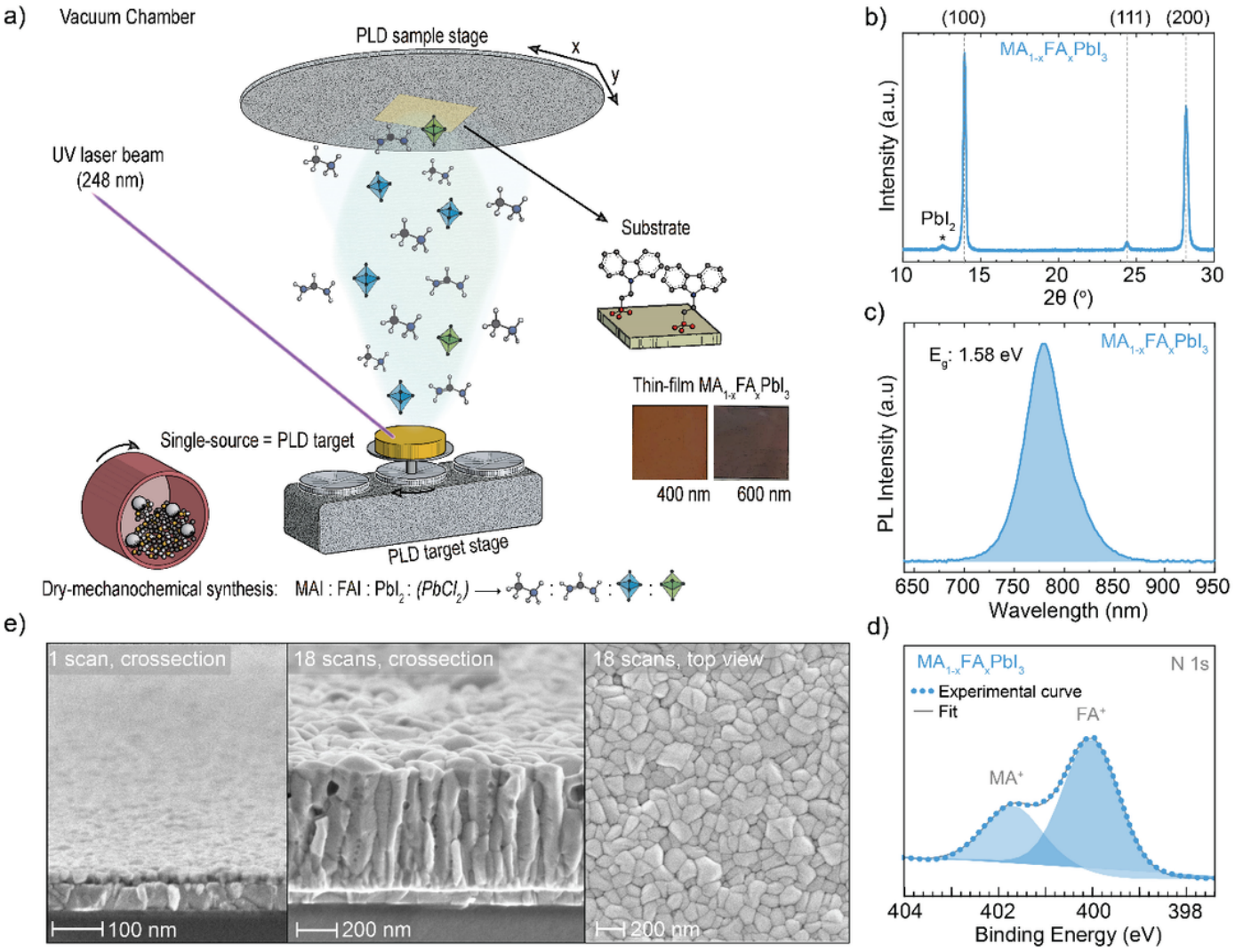

Figure 1

Structural, optical, compositional, and morphological analysis of pulsed laser deposited $MA_{1-x}FA_xPbI_3$ thin films on 2PACz-SAMs/ITO. a) Schematic representation detailing the deposition of MHP thin films by PLD starting from a dry-mechanochemical mixture of the desired precursors pressed into a PLD target and laser ablation of it to form thin films. **b)** Specular XRD pattern of a ~ 400 nm thick $MA_{1-x}FA_xPbI_3$ film displaying the (100) and (111) plane orientation. **c)** PL spectrum after excitation with a 520 nm laser, indicating a ~ 1.58 eV bandgap. **d)** High-resolution XPS spectrum of N 1s core level analysis exhibiting the peaks corresponding to both organic cations (MA^+: FA^+), demonstrating the successful incorporation and integrity of the organic molecules. **e)** SEM images of $MA_{1-x}FA_xPbI_3$ films after 1 (~20 nm) and 18 (~400 nm) deposition scans revealing a homogenous coverage from the initial growth stages, a

columnar apparent grain structure, with sizes ranging from ~ 50-100 nm and some voids discernible in thick samples, which requires improvements in the growth strategies to diminish them.

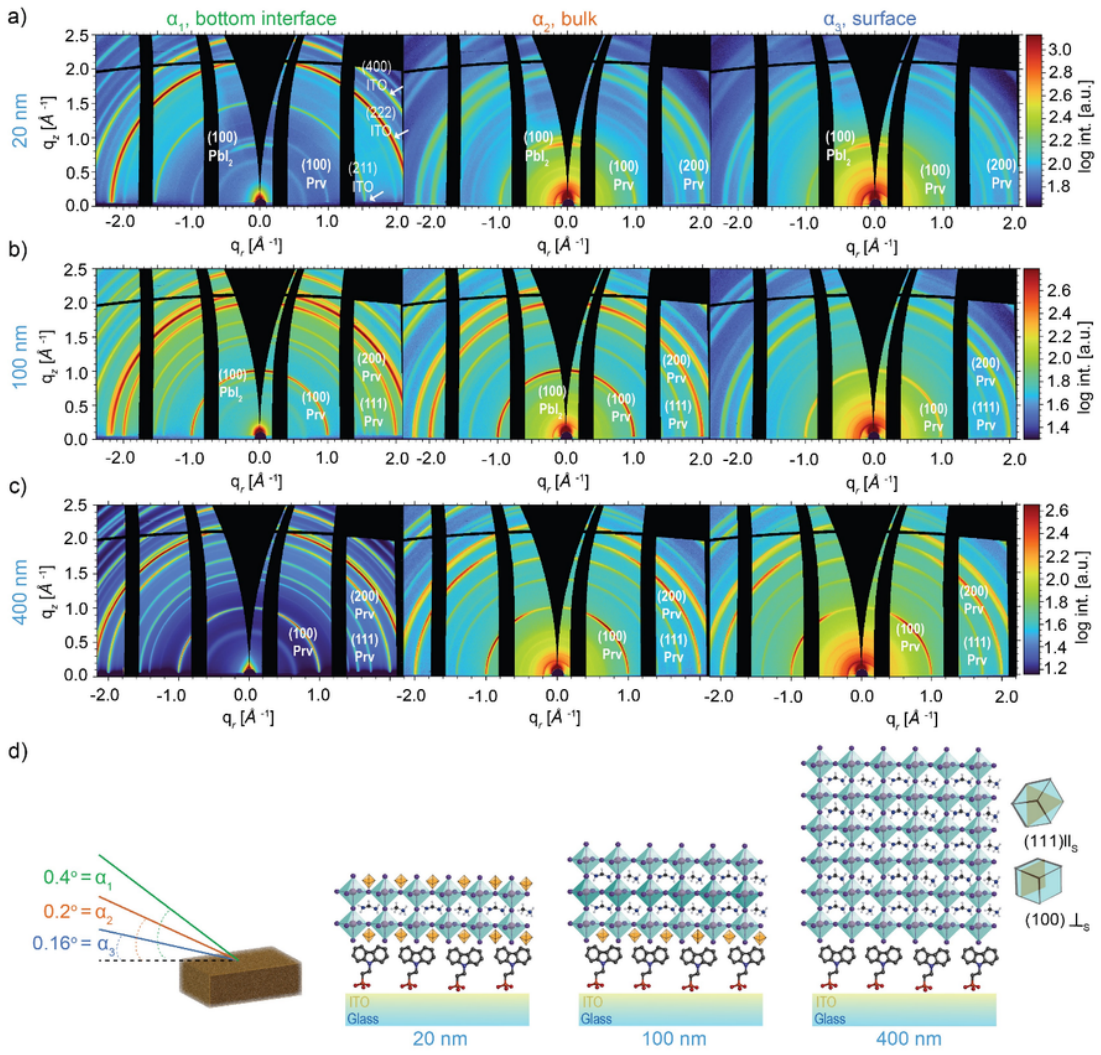

Figure 2

Depth-dependent grazing-incidence wide-angle X-ray scattering (GIWAXS) images of pulsed laser deposited $MA_{1-x}FA_xPbI_3$ thin films on ITO/2PACz-SAMs/ substrates at varying growth stages: 20, 100, and 400 nm of film thickness. A) Angle-dependent 2D GIWAXS data acquired from 20 nm (1 scan) halide perovskite films uncovering the presence of PbI_2 and low-intensity signals of the (100) perovskite planes. **b)** Angle-dependent 2D GIWAXS data of 100 nm (4 scans) halide perovskite films demonstrating a partial conversion of PbI_2 into the perovskite material as evidenced by the emergence of signals related to (100), (110), (111), and (210) perovskite planes. **c)** Angle-dependent 2D GIWAXS data for 400 nm halide perovskite films proving a full conversion of the MHP predominant in the (111) plane parallel to the substrate surface. d) Simplified schematic of the angle-dependent GIWAXS measurements, focusing close to three regions: the interface perovskite/SAMs/ITO (α_1 = 0.4°), the bulk (α_2 = 0.2°), and the surface (α_3 = 0.16°); an overview of PbI_2 presence represented by yellow octahedrons (illustrations of the partially ordered crystallite preferential orientation (100) and (111) with respect to the substrate).

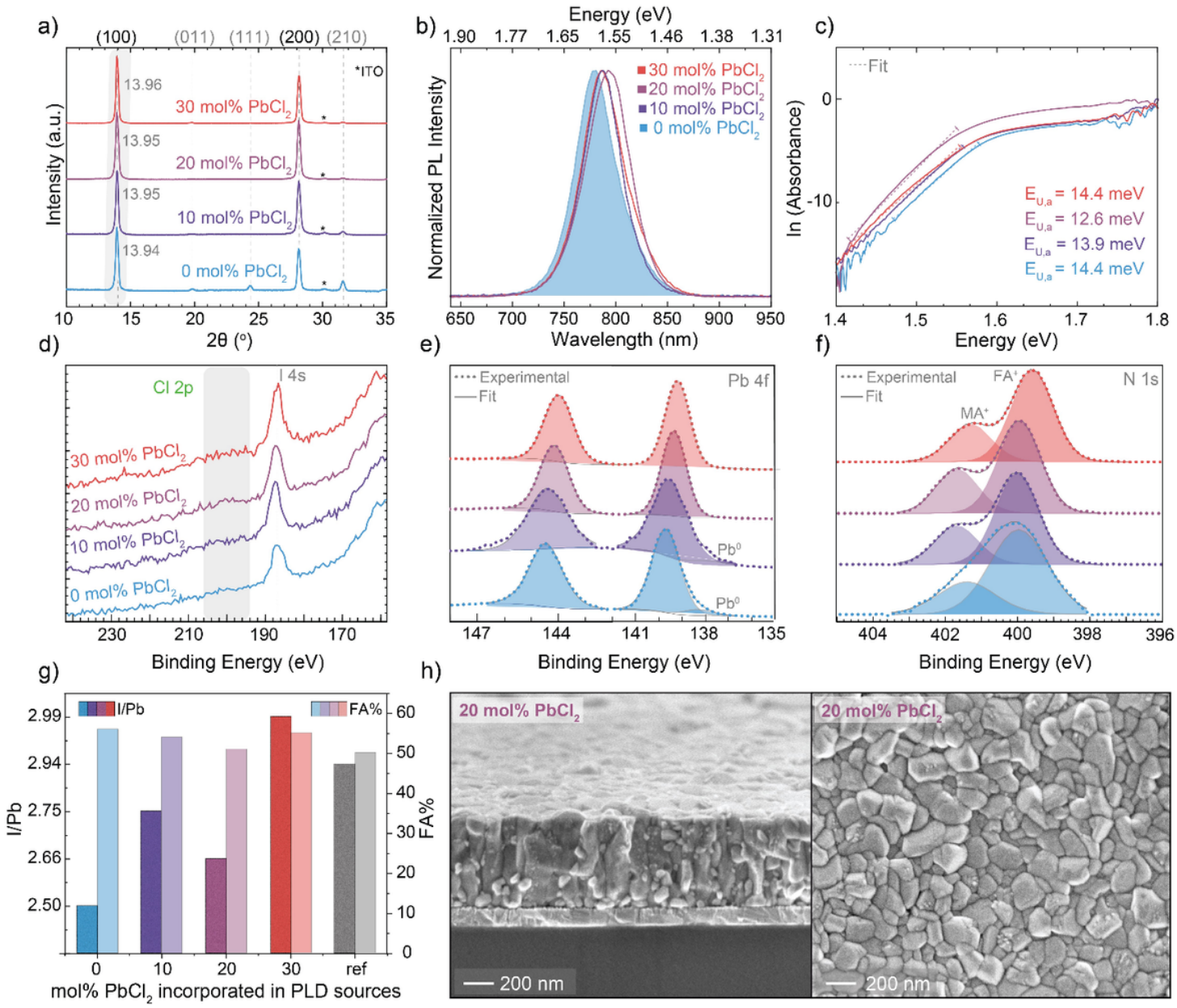

Figure 3

Structural, optical, compositional, and morphological analysis of pulsed laser deposited $MA_{1-x}FA_xPbI_3(Cl)_y$ thin films on SAMs. a) Specular XRD diffraction pattern of $MA_{1-x}FA_xPbI_3(Cl)_y$ thin films grown from PLD sources containing different $PbCl_2$ content, ranging from 0 to 30 mol%. **b)** PL emission spectra of thin films displaying a subtle redshift in films grown from PLD sources containing $PbCl_2$. **c)** E_U extraction from PL data employing the fundamental reciprocity relation between absorption and emission properties of semiconductors. **d)** Binding energy region corresponding to the Cl 2p core levels exposing no detectable signals of Cl^- in the thin film samples. **e)** Pb 4f core levels region fitted in two contributions at 139.4 ± 0.2 and 144.2 ± 0.2 eV attributed to lead bonding with iodine (Pb-I) exhibiting symmetrical peaks reflecting the homogeneity of the films. **f)** N 1s core level spectra displaying contributions corresponding to MA^+ and FA^+ cations from targets with the same MA^+: FA^+ ratios but varying $PbCl_2$

content. **g)** Bar charts representing a slight fluctuation of the FA^+ % ranging from 52-56% alongside an important variation in the I/Pb ratio on thin films grown from sources with varied $PbCl_2$ content. A reference pressed power of $MA_{50}FA_{50}PbI_3$ (grey bar, ref) is used for comparison. **h)** Cross-section and top-view SEM images of compact and void-free $MA_{1-x}FA_xPbI_3(Cl)_y$ thin films deposited from a 20 mol% $PbCl_2$ source.

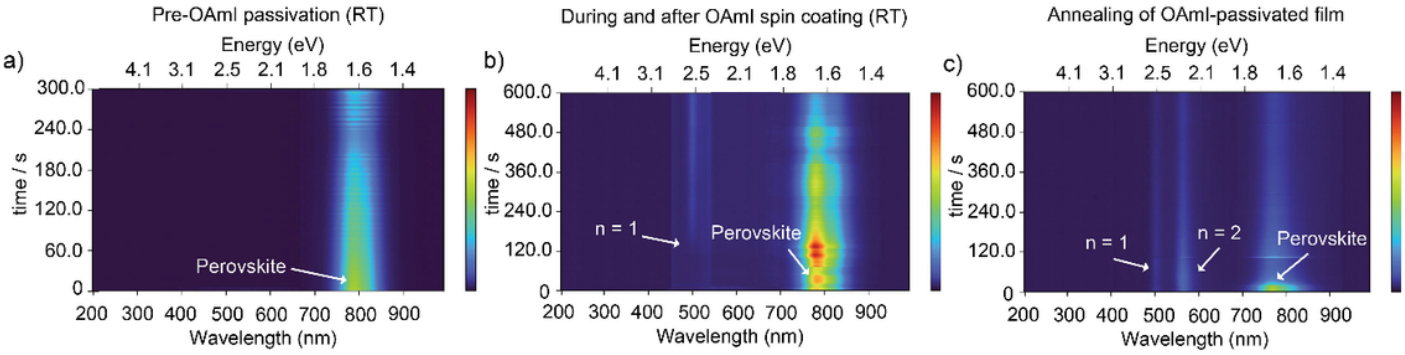

Figure 4

***In-situ* PL analysis of $MA_{1-x}FA_xPbI_3(Cl)_y$ thin film grown from 20 mol% $PbCl_2$ source using a 405 nm laser.** *In-situ* PL at **a)** RT over 5 min before OAmI passivation, **b)** during spin coating (~1 min) and the following 9 min at RT after spinning, **c)** during 10 min of annealing at 100 °C after OAmI post-treatment.

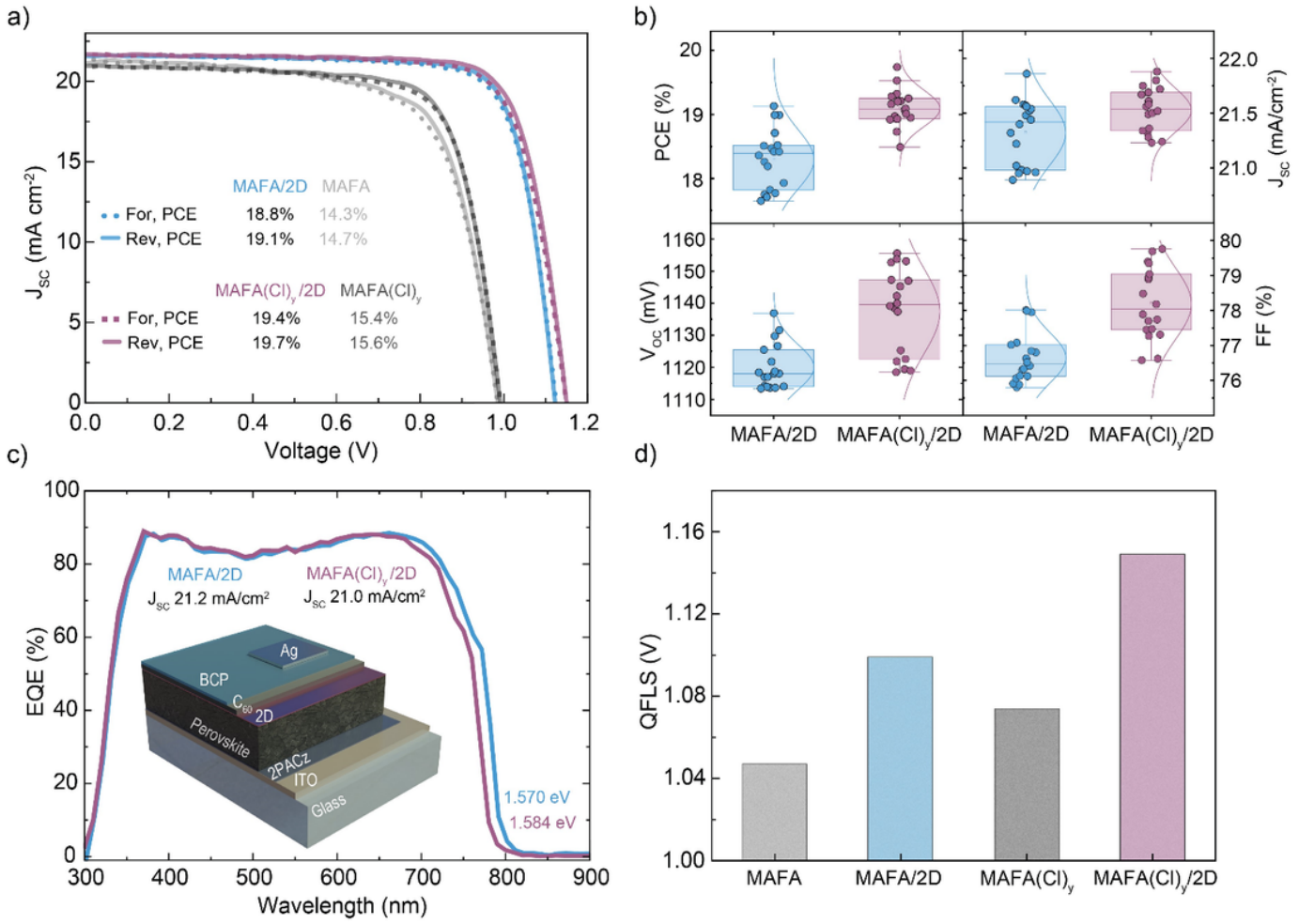

Figure 5

Performance of solar cells containing PLD-$MA_{1-x}FA_xPbI_3$ and $MA_{1-x}FA_xPbI_3(Cl)_y$ absorbers employing single source targets with 0 and 20 mol% of $PbCl_2$, respectively. a) Current-voltage (J-V) measurements of the above-mentioned photovoltaic devices under AM1.5 illumination, as measured under reverse bias (solid line) and forward bias (dashed line). **b)** Box plots representing the J-V characteristics obtained from the batch of samples containing the champion cells. **c)** External quantum efficiency (EQE) spectra of a device containing PLD-$MA_{1-x}FA_xPbI_3$ (referred as MAFA in the figure) and $MA_{1-x}FA_xPbI_3(Cl)_y$ (referred as $MAFA(Cl)_y$ in the figure) from a 0 and 20 mol% $PbCl_2$ source and the corresponding integrated J_{SC} and bandgaps, inset: schematic representation of the device stack used in this study. **d)** QFLS of ITO/2PACz/PLD-perovskite/C_{60} stack from the measured average devices.

Device stability and state-of-the-art PCE of single-source vapor deposited MHP solar cells

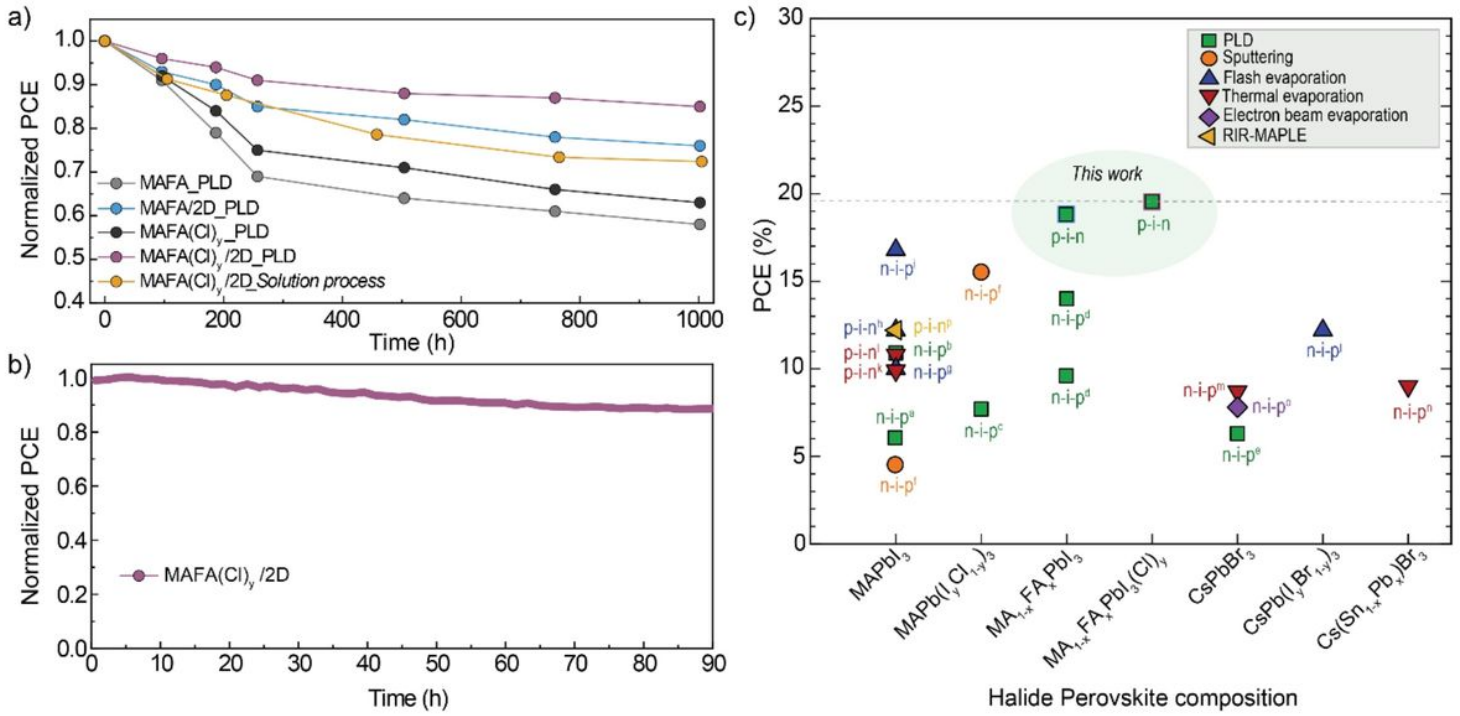

Figure 6

Stability tests of devices by PLD and state-of-the-art PCE of single-source vapor deposited MHP solar cells reported. a) Thermal stability test at 85 °C for over 1000 hours and comparison with solution-based process. **b)** MPP tracking for over 90 hours of devices containing 2D-passivated PLD-grown $MA_{1-x}FA_xPbI_3(Cl)_y$ (referred as MAFA(Cl)$_y$ /2D in the figure) from a 20 mol% $PbCl_2$ source. **c)** State-of-the-art solvent-free single-source vapor deposition methods of various halide perovskite absorber compositions and the corresponding reported PCE; references for the points in the graph are given in Supplementary Table 3.

Supplementary Files

This is a list of supplementary files associated with this preprint. Click to download.

- SIPulsedLaserDepositedPerovskiteSolarCellswith19Efficiencypreprint.docx